Functionalization of MCM-41 with titanium oxynitride deposited via PECVD for enhanced removal of methylene blue

Amr Nada, Maged Bekheet, Stéphanie Roualdes, Aleksander Gurlo, André Ayral

Functionalization of MCM-41 with titanium oxynitride deposited via PECVD for enhanced removal of methylene blue

Amr A. Nada,[a,b,*] Maged F. Bekheet,[c,d] Stéphanie Roualdes,[b] Aleksander Gurlo,[c] and André Ayral[b]

[a] Dept. of Analysis and Evaluation, Egyptian Petroleum Research Institute, Cairo, Nasr city P.B. 11727, Egypt.

[b] Institut Européen des Membranes IEM, UMR 5635, ENSCM, Université de Montpellier, CNRS, Place Eugène Bataillon, CC047, F-34095 Montpellier Cedex 5, France.

[c] Fachgebiet Keramische Werkstoffe / Chair of Advanced Ceramic Materials, Institut für Werkstoffwissenschaften und -technologien, Technische Universität Berlin, Hardenbergstraße 40, 10623 Berlin, Germany

[d] Department of Material Science Engineering, University of Utah, 122 Central Campus Dr., Salt Lake City, UT 84112, USA

Abstract

TiON and TiO_2 were grafted onto the surfaces of mesoporous silica MCM-41 by plasma enhanced chemical vapour deposition (PECVD). The results of small-angle X-ray diffraction (SAXRD), X-ray diffraction, X-ray photoelectron spectroscopy, transmission electron microscopy, and nitrogen physisorption revealed that the mesoporous structure of MCM-41 was retained and the pore size reduced from 2.46 nm to 2.19 nm and 2.18 nm after grafting of amorphous TiO_2 and TiON, respectively. In consequence, the pore volume and BET surface area decreased. These results indicate the deposition of TiO_2 and TiON particles on the surface of MCM-41, leading to partial blockage of its pores. The grafted materials were found to be effective adsorbents for methylene blue dye. The results of batch adsorption experiments at pH 7 demonstrated that TiON@mSiO_2 nanocomposite showed the highest adsorption capacity in comparison with MCM-41 and TiO_2@mSiO_2, which is due to its highly negative zeta potential at neutral conditions. The equilibrium adsorption process fits well with the Langmuir isotherm model and the calculated maximum adsorbed quantity q_{max} was found to be 129 mg/g. The pseudo-second order model best represents the adsorption kinetics data. Accordingly, the TiON@mSiO_2 nanocomposite can be used for the purification of wastewater from toxic organic dyes such as methylene blue.

Keywords: PECVD, MCM-41, Dye adsorption, Water purification, mesoporous nanocomposite.

Title Page Footnote:

_____

*Corresponding author. Email: chem_amr@yahoo.com and amr.nada@umontpellier.fr

1. Introduction:

The remediation of wastewater from dyes is a recurring challenge. Textile dyes and other industrial dyestuffs coming from the paper, leather, cosmetic and printing industries are of environmental concern due to the release of toxic and potential carcinogenic materials into water [1-6]. Wastewater produced by the dye industry, which contains harmful organic pollutants, is often discharged directly into natural bodies of water, such as rivers, or are percolated into groundwater [7-9]. The removal of these organic pollutants has recently attracted considerable attention due to their public health damage and environmental toxicity [10]. Accordingly, much attention has been paid to the development of adsorption techniques through which molecules can be rapidly removed at low cost [11-14].

Mesoporous materials, which show high adsorption affinity towards several organic and inorganic pollutants, are applicable in many industrial processes [15-18]. Among them, mesoporous silica, exhibiting high specific surface area, tunable pore size, low density, and hydrophilic surfaces, is a very promising candidate for oil refining, gas sensors, catalyst support and waste treatment [18-22]. Moreover, mesoporous silica can be easily dispersed in several solvents as well as functionalized by several hydrophilic groups/materials due to the presence of surface hydroxyl groups [23-25]. For example, the catalytic and adsorptive properties of mesoporous silica, in particular Mobil Composition of Matter (MCM) and Santa Barbara Amorphous type materials (SBA), can be enhanced by grafting with transition metal oxides such as TiO_2, Fe_2O_3 and SnO_2 [26-28].

Two common approaches for functionalizing surfaces of mesoporous silica are: (i) post-grafting (post modification) procedures [23-25] and (ii) direct-grafting (direct co-condensation) through the co-polymerization of a silica precursor [21, 29]. Despite the fact that direct-grafting is fast and takes place in one step, materials produced by this method exhibit a less ordered mesoporous structure and low specific surface area in comparison with those produced by the post-grafting method. Additionally, the pore structure as well as the specific surface area can be well controlled in the post-grafting method which is usually used to functionalize the surface of mesoporous silica with organic materials via the reaction with –OH groups on their surface. Up to now, tremendous efforts have been devoted to apply the

post-grafting method in the synthesis of multifunctional mesoporous silica composites with improved catalytic and adsorption properties for effective wastewater treatment [23-25].

In this study, the composites TiO_2@mSiO_2 and TiON@mSiO_2 were prepared by grafting MCM-41 with TiO_2 and TiON, respectively, by plasma enhanced chemical vapour deposition (PECVD). The adsorptive properties of the obtained composites were investigated and compared to the unfunctionalized MCM-41 silica. PECVD technique has been recently applied for the preparation of TiO_2/MCM-41 composites [30] in several steps by coating the MCM-41 powder first on silica wafer as substrate before the deposition of TiO_2 by PECVD at 500°C. The obtained composites were further annealed at 700°C. On the other hand, no reports about using PECVD technique for grafting mesoporous silica with TiON. TiN/MCM-41 composites were previously prepared by heat-treatment under ammonia gas at $T \geq 600$°C for very long time (i.e. 24 hrs) [31]. However, these high preparation temperatures are energy consuming and might result in the collapse of the hexagonal pore structure of MCM-41 and reduction in its surface area, which may reduce its adsorptive properties. Accordingly, the main goal of this work to modify the set-up of PECVD technique to deposit TiO_2 and TiON directly on MCM-41 powders at much lower temperatures (i.e. 150 °C) relative to those used in the previous works [30, 31].

2. Experimental:

2.1. Chemicals

Cetyltrimethylammonium bromide (CTAB, 99%, Sigma-Aldrich), titanium tetra-isopropoxide (TTIP, 97%, Sigma-Aldrich), ammonia solution in water (~30%, Sigma-Aldrich), tetraethoxysilane (TEOS, 99.99%, Sigma-Aldrich), ethanol (absolute, Honeywell) and methylene blue (Sigma-Aldrich) were used without further purification.

2.2. Synthesis of MCM-41

MCM-41 was synthesized by a modified heterogeneous system [32] as follows: 2.5 g of CTAB as templating agent was dissolved in 50 mL of deionized water at 30 °C, followed by the addition of 22 mL of aqueous ammonia hydroxide solution (30% NH_4OH) and 60 mL of absolute ethanol under continuous stirring. The dropwise addition of 5 mL of tetraethoxysilane to the surfactant solution resulted in the formation of a gel that turned into a white precipitate after stirring for a further two hours. The obtained white precipitate was filtered and washed

with deionized water and ethanol. After drying at room temperature, the sample was heated to 550 °C with heating rate 1 °C/min in air and kept at this temperature for 5 h to remove the template.

2.3. Preparation of TiO_2@mSiO_2 and TiON@mSiO_2

The grafting of TiO_2 and TiON at MCM-41 surface was performed by the PECVD technique (Figure **1**) according to the following procedure: (i) the deposition chamber was first evacuated to 1 Pa using a vacuum pump; (ii) 1 g of MCM-41 powders were inserted into stainless steel dish to act as deposition substrate (i.e. bottom electrode) and heated to 150°C by using a heating device (Eurotherm); (iii) the Ti-based precursor was introduced into the deposition chamber by passing Ar as carrier gas through hot titanium (IV) isopropoxide solution at 80°C in an oil bath, while the carrying line was heated at 100 °C in order to avoid any condensation of the precursor; (iv) oxygen gas was simultaneously introduced as an oxidant during the deposition process; (v) the plasma was generated inside the deposition chamber using an R.F. power generator (CESAR^{TM} 136) coupled with a matching box (RF Navio, Advanced Energy) that is connected to an inner electrode (diameter 10 cm) on top of the chamber, while the bottom electrode (diameter 10 cm) and body of the chamber were grounded; (vi) the non-reactive species were retained during the deposition process by a cold trap placed between the deposition chamber and the vacuum pump. All deposition experiments were performed using discharge power of 50 W for 60 min (the powder was mixed in the dish every 20 min to insure better homogeneity of the deposit on the particles) at constant partial pressure of oxygen gas P_{O2} and TTIP + Ar mixture ($P_{Ar + TTIP}$) of 10 Pa and 30 Pa, respectively, while the distance between both electrodes (d_P) was 3.0 cm. TiON@m-SiO_2 was prepared by applying ammonia gas with constant partial pressure of 10 Pa in addition to oxygen and TTIP + Ar mixture gases. Then the prepared samples were calcined at 350 ^oC with rate 1 ^oC/min for 4 hours in air.

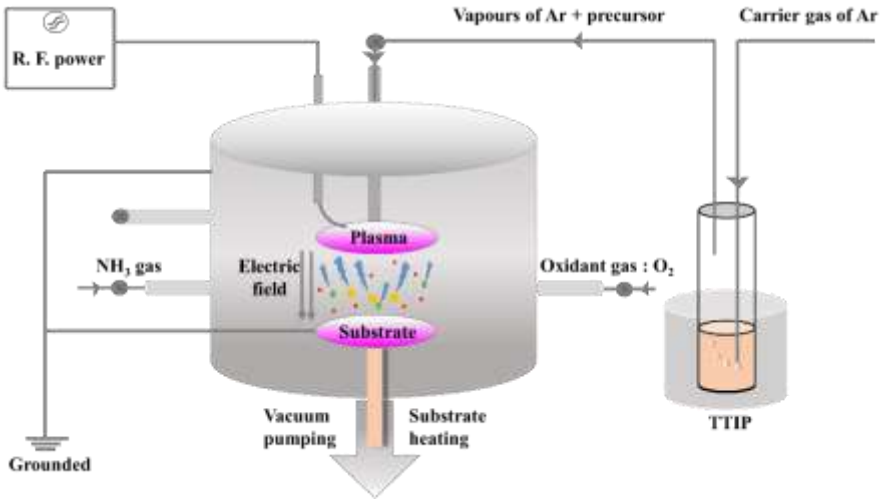

Figure 1. Schematic drawing of PECVD technique used for preparing TiO_2@mSiO_2 and TiON@mSiO_2 samples.

2.4. Characterization

The prepared MCM-41 as well as TiO_2@mSiO_2 and TiON@mSiO_2 samples were characterized using small-angle X-ray diffraction (SAXRD) using a Bruker AXS D8 ADVANCE with a Lynx Eye 1D detector (Bruker, Germany). Measurements were performed in a Bragg–Brentano geometry using a $CuK_{\alpha 1}$ radiation wavelength of 0.154 nm at 35 kV and 40 mA. All the patterns were collected using a step time of 1 s/0.0003°. The crystalline phase of the materials was analysed by wide-angle X-ray diffraction (WAXRD) using a PANAlytical Xpert-PRO diffractometer (PANalytical, Netherlands) equipped with an Xcelerator detector and Ni-filtered $CuK_{\alpha 1}$ (λ = 0.154 nm) radiation. The scan step size was fixed at 0.0167°/step and the time per step was 0.55 sec/step. The elemental composition and oxidation environment of Ti on the prepared samples were investigated by X-ray photoelectron spectroscopy (XPS) on an Escalab 250 (Thermo Fisher Scientific, USA) using a monochromatic Al K Alpha (1486.6 eV) at 2kV and 1 µA. 400 µm of the surface diameter was analysed with acquisition times of 1203.5 s. The XPS spectra were calibrated to C1s at 284.8 eV. Energy-dispersive X-ray spectroscopy analysis (EDX) was performed with a Zeiss EVO HD15 microscope (Zeiss, Germany) coupled with an Oxford X-MaxN EDX detector. The morphology of all samples was studied via transmission electron microscopy (TEM) on JEOL JEM 2100 (JEOL, Japan) at an accelerating voltage of 200 kV. The samples were prepared by dispersing a small amount of the powder in ethanol by ultrasonic treatment for 30 minutes. A drop of the suspension was applied to a copper grid covered with a holey carbon film. The pore size and specific surface

area were studied with nitrogen sorption analysis. Nitrogen adsorption-desorption isotherms were recorded at 77 K on a NOVA 3200 apparatus (Quanta-chrome Corporation, USA) after degassing for 10 h at 200 °C under vacuum. Surface area was determined using the Brunauer, Emmet and Teller (BET) method and was calculated from multi-point at relative pressure (P/Po) range from 0.05 to 0.30. The pore size distribution was obtained from the Barrett, Joyner and Halenda (BJH) method using the adsorption points of the isotherm. Zeta potential measurements were carried out on Zetasizer Nano ZS (Malvern Instruments, Malvern, UK), where all samples were dispersed in water at room temperature (i.e. 25^{o} C). The FT-IR spectra of the samples dispersed in KBr pellets were recorded by using the 670 FT-IR spectrometer (Varian) in the range 400 - 4000 cm^{-1} with the resolution 4 cm^{-1}.

2.5. Adsorption experiments

2.5.1. Batch equilibrium studies

An aqueous stock solution with a concentration 1000 mg/L of methylene blue (MB) dye was first prepared by dissolving 1g of the dye in 1 L distilled water. The solutions were further diluted to different concentrations in 1L flasks. Adsorption experiments were carried out in 100 mL flasks in which 25 mL of aqueous dye solutions with different concentrations (100-500 mg/L) were placed in the dark in order to avoid MB degradation by direct photolysis or by photocatalysis. The adsorbent dosages of the three samples (MCM-41, TiO_2@$mSiO_2$ and TiON@$mSiO_2$) were varied from 0.8 g/L to 2.4 g/L, while the pH of the solutions were carefully controlled between 3 and 11 by using 0.1 M HCl and 0.1 M NH_4OH solutions. The contact times were controlled in the range of 20 to 180 min. The stirring speed of 400 rpm at room temperature was maintained for all experiments. The adsorbent was separated from the dye solution after each adsorption experiment by centrifugation at 5000 rpm for 10 min. Then, the concentrations of methylene blue (MB) dye were determined from their UV-Vis absorbance according to the calibration method. A UV/VIS/NIR spectrometer (Perkin Elmer Lambda 9) was used at λ = 664 nm. The percentage of the dye that was removed (% removal) and the equilibrium adsorption capacity q_e (mg/g) were calculated as follows:

$$\%removal = \frac{(C_i - C_e)}{C_i} \times 100 \qquad (1)$$

$$q_e = \frac{(C_i - C_e)V}{m} \quad (2)$$

where C_i and C_e refer to the initial and equilibrium concentration (mg/L), respectively, of the dyes solutions, m is the weight of adsorbent (g) and V is the volume of dyes solutions (L).

2.5.2. Adsorption isotherms

The adsorption isotherms of MB dye onto TiON@SiO_2 sample were simulated using different models, namely, Langmuir, Freundlich and Tempkin isotherms. The nonlinear form of Langmuir isotherm model [33] is described in the Eq. S1 (ESI). The nonlinear form of Freundlich model [34] is given by the Eq. S2 (ESI), while Tempkin model [35] and Dubinin–Radushkevich model [36] are represented by the Eq. S3 and Eq. S4 (ESI), respectively.

2.5.1. Adsorption thermodynamics

Thermodynamic analysis of MB dye adsorption onto TiON@SiO_2 sample was conducted by performing the adsorption experiments at different temperatures (298–338 K). The corresponding thermodynamic parameters such as the adsorption Gibbs free energy change (ΔG^0, kJ/mol), the adsorption enthalpy change (ΔH^0, kJ/mole), and the adsorption entropy change (ΔS^0, kJ/mole) were calculated according the eq. S6-S7 (ESI) [37].

2.5.2. Adsorption kinetics

Experiments to determine the kinetics of MB dye adsorption onto TiON@SiO_2 samples were carried out by adding 40 mg of the TiON@SiO_2 powder into 25 mL of MB dye solution with an initial concentration C_i = 100 mg/L. The aqueous solutions were separated at different contact times by centrifuging for UV-Vis absorbance measurements. The adsorption quantity q_t (mg/g) of the dye onto the TiON@SiO_2 sample at time t was calculated according to Eq. S8 (ESI) and adsorption kinetic data was analyzed using the nonlinear form of pseudo-first-order [38], pseudo-second-order [39], and Elovich kinetic [40] models according the Eq. S9-S11 (ESI).

3. Results and discussion

3.1. Structure, composition and porosity characteristics of MCM-41, TiO_2@$mSiO_2$ and TiON@$mSiO_2$ samples

Small angle X-ray diffraction (SAXRD) was initially used to characterize the effect of TiO_2 and TiON deposition on the structure of the MCM-41 matrix. Figure 2 a shows the SAXRD patterns of MCM-41, TiO_2@$mSiO_2$ and TiON@$mSiO_2$ samples. SAXRD pattern of MCM-41 revealed three reflections at $2\theta_{100}$ = 2.423°, $2\theta_{110}$ = 4.203° and $2\theta_{200}$ = 4.980°, which satisfy the relation for *p*6*mm* hexagonal symmetry of the ordered mesoporous MCM-41 [41]. The SAXRD patterns of TiO_2@SiO_2 and TiON@SiO_2 materials exhibit a (100) reflection, which suggests the hexagonal pore structure of MCM-41 is retained after the TiO_2 and TiON deposition. However, in comparison with MCM-41, the relative intensity of the (110) and (200) reflections are decreased compared to the (100) reflection after depositing TiO_2 and TiON, indicating the decrease in the long-range order of the pores. This could be attributed to the deposition of TiO_2 and TiON on the surface of MCM-41, leading to partial blockage of its pores. Moreover, with depositing TiO_2 and TiON on the surface of MCM-41, a small shift of (100) reflection to higher 2θ values was observed, which indicates a decrease in the interplanar distance d_{100} and the hexagonal unit cell parameter (a_0). The lattice parameter a_0 of the samples were calculated according to the formula $a_0=2d_{100}/\sqrt{3}$. The wall area (W) of the pores was also calculated using the formula $W=\frac{a_0^2\sqrt{3}}{4}-\frac{\pi D^2}{8}$ (see supporting information Figure S1), where D is the average pore diameter determined from N_2 adsorption analysis. The results (see Table 1) revealed an increase of the wall area of TiO_2@$mSiO_2$ and TiON@$mSiO_2$ in comparison with MCM-41 sample, which confirms the deposition of TiO_2 and TiON particles on the surface of MCM-41, leading to partial blockage of its pores.

Wide-angle X-ray diffraction (WAXRD) patterns (Figure 2 b) of the three samples exhibited a broad reflection between 2θ = 10° and 20°, which indicates the amorphous structure of MCM-41 support as well as the deposited TiO_2 and TiON materials.

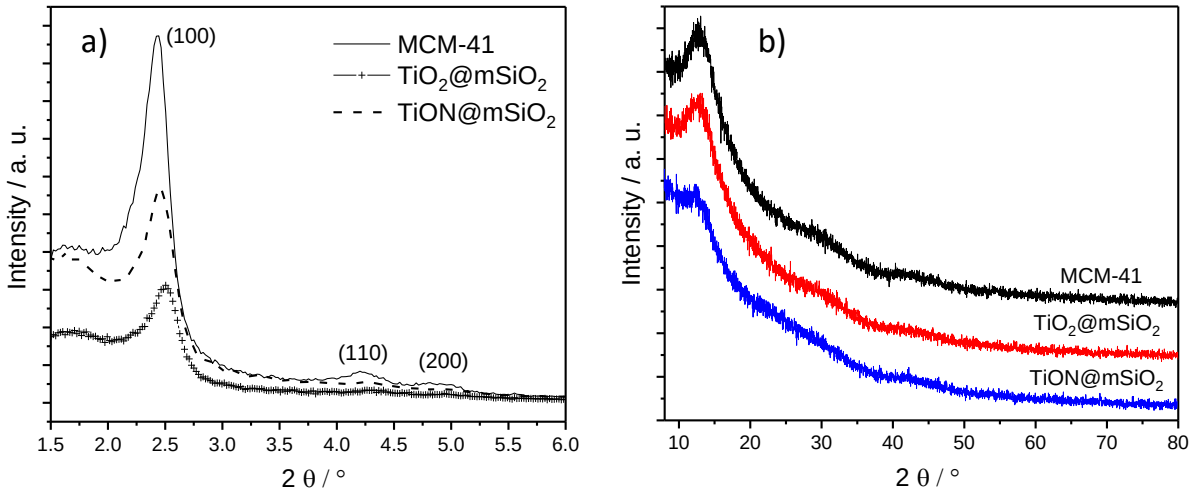

Figure 2: SAXRD (a) and WAXRD (b) patterns of MCM-41, TiO_2@$mSiO_2$ and TiON@$mSiO_2$ samples

The nitrogen adsorption–desorption isotherms and BJH pore size distributions (insets) of MCM-41, TiO_2@$mSiO_2$ and TiON@$mSiO_2$ samples are shown in Figure 3. The isotherms of the three samples can be classified as a type IV isotherms, commonly related to mesoporous materials, as established by the international Union of Pure and Applied Chemistry (IUPAC) [42]. Nevertheless, some differences were observed between the sorption curves of TiO_2@$mSiO_2$ and TiON@$mSiO_2$ in comparison with that of MCM-41 sample. The isotherm of MCM-41 exhibits a type H1 hysteresis loop with a well-defined inflection at relative low pressures (p/p_0 = 0.2-0.4), which associated with well-ordered mesoporous materials with narrow distributions of relatively uniform (cylindrical-like) pores. The inflection in the isotherm corresponds to the capillary condensation nitrogen inside the primary mesoporous and its sharpness indicates a uniform pore size distributions [22]. On the other hand, N_2-physisorption isotherms of TiO_2@$mSiO_2$ and TiON@$mSiO_2$ exhibit two regions of hysteresis between the adsorption and desorption traces, from relative pressures (p/p_0) of 0.2–0.35 and 0.40–0.60 (Fig. 8 b-c). The hysteresis at (p/p_0) of 0.2–0.35 is attributed to well-ordered mesoporous structure of MCM-41, indicating that the deposition of TiO_2 and TiON did not destroy the integrity of the mesoporous MCM-41 support. However, the inflection in their isotherms exhibits a gentle slope, suggesting the decrease in the long-range order of the pores with TiO_2 and TiON loading, which is also consistent with SAXRD results. The hysteresis loop at the relative pressure range of 0.40–0.60 shows a type H4 characteristic, which is associated with narrow slit-like pores in materials containing both micropores and mesopores [42, 43].

These results suggest the existence of the void defects in the framework of MCM-41 due to the deposition of TiO_2 and TiON particles on the surface. The BET surface area, average pore diameter and pore wall area were calculated and listed in Table 1. As shown in Table 1, the deposition of TiO_2 and TiON particles on MCM-41 surface resulted in a decrease in the pore size from ~2.5 nm to ~2.2 nm, while an increase in the wall thickness between the pores was observed. These results reveal pore blocking due to deposition of TiO_2 and TiON particles on the surface of the MCM-41 particles. Accordingly, pore volumes and BET surface area decrease significantly for TiO_2@$mSiO_2$ and TiON@$mSiO_2$ samples. However, the pore size diameter in TiO_2@$mSiO_2$ and TiON@$mSiO_2$ is still higher than 2 nm, which indicates that the mesoporosity is retained after the TiO_2 and TiON deposition.

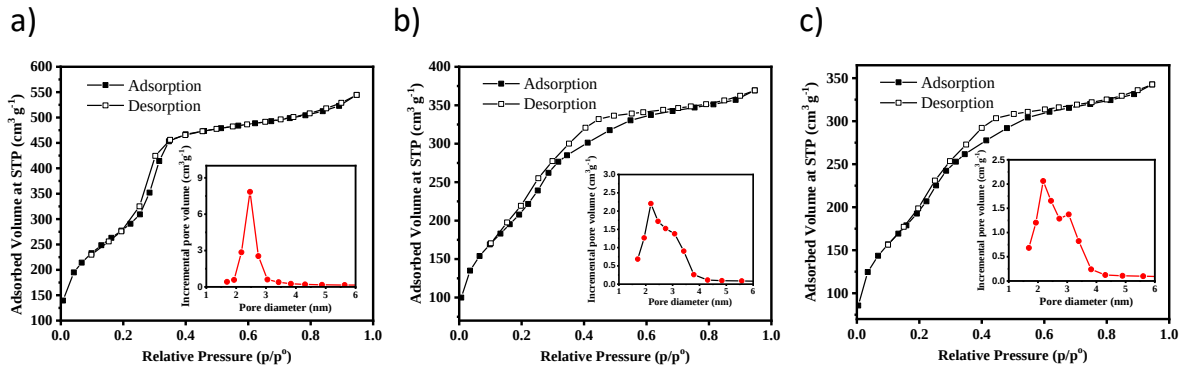

Figure 3: Nitrogen adsorption-desorption isotherms and BJH pore size distribution profiles (inset) of (a) MCM-41, (b) TiO_2@$mSiO_2$ and (c) TiON@$mSiO_2$ samples.

Table 1: Textural properties of MCM-41, TiO_2@$mSiO_2$ and TiON@$mSiO_2$ samples obtained from SAXRD and N_2 physisorption characterizations.

Samples	d_{100} (nm)	a_0 (nm)	S_{BET} (m^2/g)	Pore volume (cm^3/g)	BJH Pore Diameter (nm)	Pore wall area (nm^2)
MCM-41	3.634	4.196	1268	0.92	2.5	5.240
TiO_2@$mSiO_2$	3.535	4.082	869	0.57	2.2	5.331
TiON@$mSiO_2$	3.593	4.149	801	0.55	2.2	5.591

To study the chemical composition on the surface of the obtained samples after PECVD treatment, the three samples were investigated by X-ray photoelectron spectroscopy (XPS). As observed in Figure 4 a, the fully scanned spectra demonstrated that Si, O and C existed in pure MCM-41. The C in pure MCM-41 could have originated from the CTAB surfactant used as a

pore template. In addition to the previous elements, Ti was observed in TiO_2@$mSiO_2$ sample, while Ti and N were detected in the surface of the TiON@$mSiO_2$ sample. Subsequently, the O1s high-resolution XPS spectra of the MCM-41, TiO_2@$mSiO_2$ and TiON@$mSiO_2$ were analyzed in Figure 4 b. The O1s spectrum of pure MCM-41 exhibits an asymmetric band that consists of two peaks. The main peak at 533.2 eV can be assigned to oxygen from Si-O-Si bonds, while the other low intensity peak at 534.7 eV can be attributed to the surface silanol Si-OH groups. These two peaks are slightly shifted to lower binding energies for theTiO_2@$mSiO_2$ and TiON@$mSiO_2$ samples, which could be due to the formation of Si-O-Ti bonds [22]. Furthermore, an additional peak was observed at about 529.8 eV, which can be ascribed to oxygen lattice in anatase (TiO_2). Next, the deposition of TiO_2 on the surface of MCM-41was confirmed from the Ti2p spectra of TiO_2@$mSiO_2$ and TiON@$mSiO_2$ (Figure 4 c). In the Ti2p spectrum of TiO_2@$mSiO_2$, the doublet peak $Ti2p_{3/2}$ and $Ti2p_{1/2}$ appear at 458.3 and 464.1 eV, respectively, arises from spin orbit-splitting. These two peaks correspond to Ti^{4+} in the TiO_2 lattice [44]. Additionally, the shoulders $Ti2p_{3/2}$ at 460.2 eV and $Ti2p_{1/2}$ at 465.8 eV are consistent with Ti^{3+} cross-linked in the silica network [22]. These peaks were slighted shifted by about 0.2 eV to higher binding energies for the TiON@$mSiO_2$ sample. Moreover, the intensities of the shoulders $Ti2p_{3/2}$ slightly decreased, which suggests the incorporation of N in the TiO_2 lattice during the deposition process. The observed peak at 397.6 eV in the N1s spectrum of TiON@$mSiO_2$ (Figure 4 d) further confirms the formation of titanium oxynitride on the surface of MCM-41 [45]. The Ti/Si mole ratios measured from XPS spectra are 0.06 and 0.11% in the TiO_2@$mSiO_2$ and TiON@$mSiO_2$ samples, respectively. However, EDX analysis reveals Ti/Si mole ratios of 0.08 and 0.09 in TiO_2@$mSiO_2$ and TiON@$mSiO_2$, respectively.

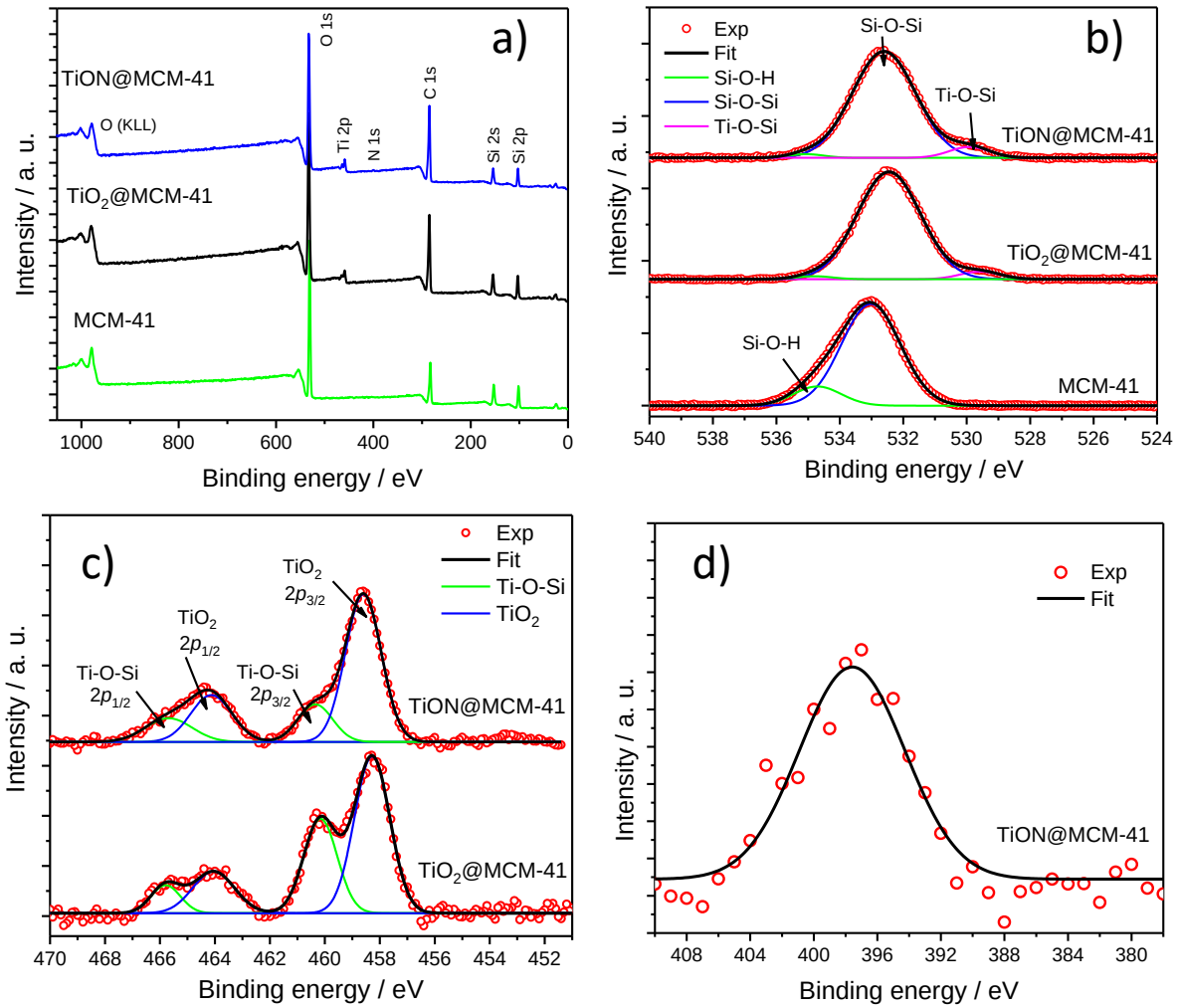

Figure 4: XPS survey spectra (a) and high-resolution XPS spectra of O1s (b), Ti2p (c), and N1s (d) for MCM-41, TiO_2@mSiO_2 and TiON@mSiO_2 samples.

Transmission electron microscopy (TEM) characterization was used to examine the pore structure and morphology of all samples. Figure 5 shows the TEM images of MCM-41, TiO_2@mSiO_2 and TiON@mSiO_2 samples. As shown in Figure S2 and Figure 5 a, MCM-41 exhibits long-range pore ordering. Uniform black spots are observed in the TEM images of TiO_2@mSiO_2 and TiON@mSiO_2 (Figure 5 b and c), which correspond to deposited TiO_2 and TiON particles on the surface of MCM-41. The average size of TiO_2 and TiON particles are 15 ± 1 and 18 ± 1 nm, respectively. As shown in Figure S2 and Figure 5 b and c, the porous structure was maintained after the deposition of TiON on the surface of MCM-41, which is consistent with SAXRD results.

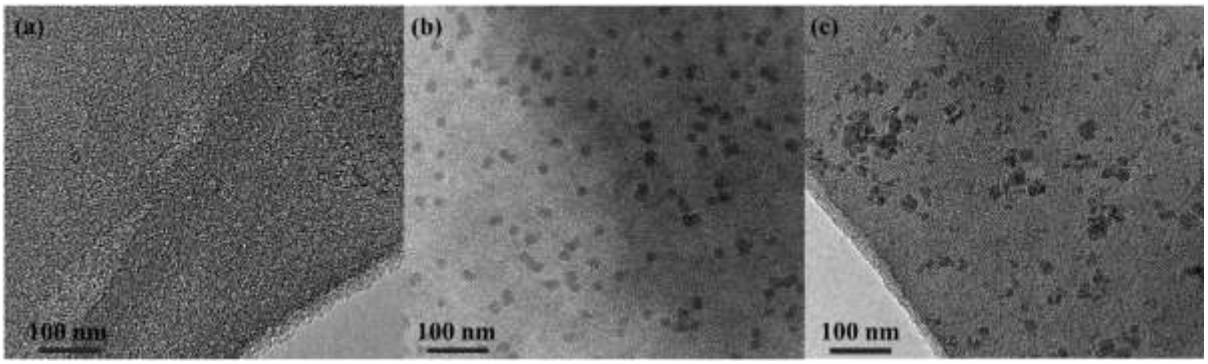

Figure 5: TEM images of (a) MCM-41, (b) TiO_2@$mSiO_2$ and (c) TiON@$mSiO_2$ samples.

The deposition of TiO_2 and TiON on the surface of MCM-41 was also confirmed by pH-dependent zeta potential measurements. Figure 6 shows the surface zeta potential as function of pH for MCM-41, TiO_2@$mSiO_2$ and TiON@$mSiO_2$ samples. The isoelectric point (IEP) of unmodified MCM-41 was observed at pH 3.2, which is good agreement with previous reported values (pH 3.1) [46]. IEPs of TiO_2@$mSiO_2$ and TiON@$mSiO_2$ have been shifted to slightly higher values (pH 3.9 and 3.6 for TiO_2@$mSiO_2$ and TiON@$mSiO_2$, respectively) in comparison with that of MCM-41. This result is consistent with previous work, which reports that oxides with highly electronegative ions (e.g. Si) show IEP at lower pH values in comparison with those with low electronegative ions (e.g. Ti) [47]. At pH lower than their pH_{ZPC} values, the zeta potentials of three materials were positive, which may be due to the protonation of the –OH groups on the surface of the mesoporous silica or TiO_2 particles in the acidic solution. At high pH values, free hydroxide groups, which are prevalent in basic solutions, can deprotonate the –OH groups on the surfaces of SiO_2 and TiO_2, resing in a negatively charged surface. However, TiO_2@$mSiO_2$ and TiON@$mSiO_2$ samples exhibit strongly positive zeta potentials at lower pH and strongly negative zeta potentials at higher pH values in comparison to that of the unmodified MCM-41. These results can be explained by the electronegativity of silicon and titanium ions, which can affect the strength of the O-H bonds on SiO_2 and TiO_2. Additionally, the N-H bonding in TiON@$mSiO_2$ is weaker than the O-H bonding as the electronegativity of nitrogen (3.0) is less than that of oxygen (3.5). Therefore, TiON@$mSiO_2$ showed the highest negative zeta potential in the basic solutions because N-H sites act as acidic sites. This result is also in good agreement with recent studies which show that the surface zeta potential of TiO_2 becomes more negative as the amount of nitrogen doping increases [48].

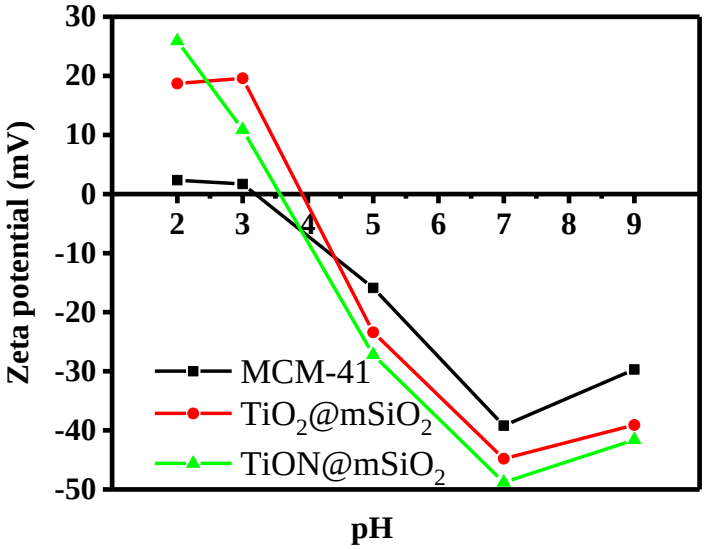

Figure 6: Zeta potential of MCM-41, TiO_2@$mSiO_2$ and TiON@$mSiO_2$ samples as function of pH.

3.2. Adsorption of methylene blue

To study the effect of TiO_2 and TiON on the adsorption capacity q_e (mg/g) of MCM-41, batch adsorption experiments of methylene blue dye from aqueous solutions were conducted on MCM-41, TiO_2@$mSiO_2$ and TiON@$mSiO_2$ samples. Figure 7 shows the equilibrium concentration of MB remaining in the water after 2 h of adsorption experiments using MCM-41, TiO_2@$mSiO_2$ and TiON@$mSiO_2$ samples with dosage of 1.6 g/L at pH value of 7.0 at room temperature. As shown in Figure 7, the remaining concentration of MB dyes in the water are very low when TiON@$mSiO_2$ and TiO_2@$mSiO_2$ are used as adsorbents. Accordingly, TiON@$mSiO_2$ and TiO_2@$mSiO_2$ samples show higher equilibrium adsorption capacities q_e of 60 and 37 mg/g, respectively, than that of MCM-41 sample (19 mg/g). These results can be explained by changing the surface charge of MCM-41 due to the deposition of TiO_2 and TiON on the surface. As shown in Figure 6, the surface charges of TiON@$mSiO_2$ and TiO_2@$mSiO_2$ are more negative than that of MCM-41, therefore, the positively charged groups $(=N(CH_3)_2)^+$ of MB dye could be easily electrostatically attracted by TiO_2 and TiON particles on the surface of MCM-41. Since TiON@$mSiO_2$ sample shows the highest adsorption capacity of the three samples, this sample was chosen for further adsorption experiments.

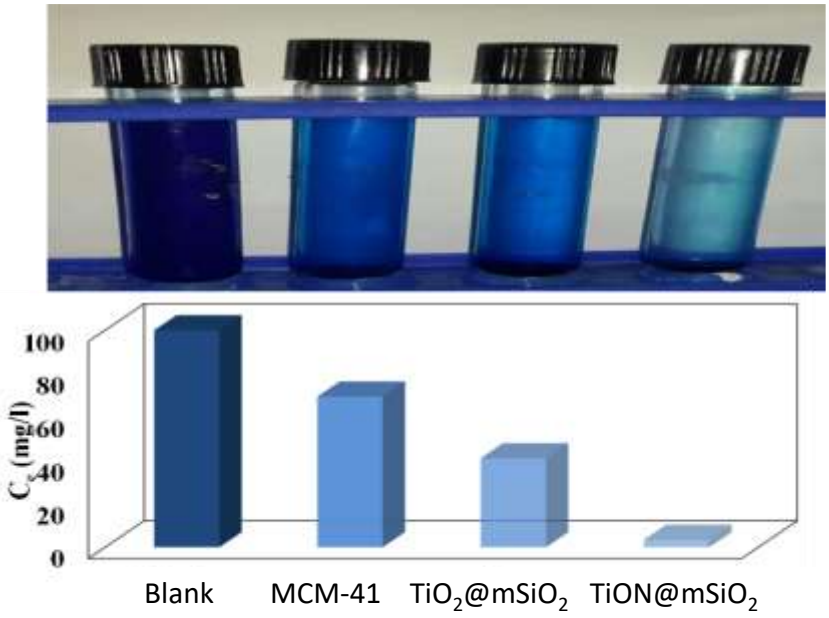

Figure 7: Equilibrium concentration C_e of MB after adsorption experiments using (a) MCM-41, (b) TiO_2@$mSiO_2$ and (c) TiON@$mSiO_2$ samples with dosage of 1.6 g/L at equilibrium time of 2 h and pH value of 7 at room temperature. The blank sample refers to the initial concentration of the dye (100 mg/L).

3.3. Effect of adsorbent dose and solution pH on MB dye adsorption

The influence of the amount of TiON@$mSiO_2$ on the adsorption and removal of MB dye with an initial dye-solution concentration of 100 mg/L, pH 7 and contact time of 2 h, are displayed in Figure 8 a. The removal percentage of MB significantly increased from 50% to ~97% with an increase in adsorbent dose from 0.8 to 1.6 g/L, which is due to the increase in the number of active adsorption sites as the amount of adsorbent increased [49]. The constant removal efficiency at doses more than 1.6 g/L indicates that the number of active adsorption sites no longer increases at these higher doses of adsorbent, which may be attributed to the partial aggregation of adsorbent particles at higher adsorbent doses [50]. On the other side, the equilibrium adsorption capacity remarkably decreased from 60 to 22 mg/g with an increase in adsorbent dose from 0.8 to 1.6 g/L, which is due to the limited concentration of dyes molecules needed to saturate all the active adsorption sites at these high doses of adsorbent [51]. However, the adsorbent dose of 1.6 g/L was chosen for further experiments because of the high removal efficiency as well as adsorption capacity at this adsorbent dose.

As shown in Figure 6, the surface charge of TiON@$mSiO_2$ was drastically changed with varying the pH values of the solution. Additionally, the degree of ionization and the chemical nature of MB dyes could be also affected by the pH of the solution. Therefore, the influence of pH on adsorption capacity and removal of cationic MB dye with initial dye-solution concentration of 100 mg/L onto TiON@$mSiO_2$ sample at dosage of 1.6 g/L and contact time of 2 h was studied (Figure 8 b). It can be seen that an increase in the solution pH from 3 to 7 resulted in a remarkable increase in the adsorption capacity of MB dye from 22 to 60 mg/g as well as removal efficiency from 35.3% to 96.6%. However, the adsorption capacity and removal efficiency did not change significantly with a further increase in the solution pH above 7. These results can be explained by the variation of surface charges of adsorbent and MB dye with solution pH. As shown in Figure 6, the surface charge of TiON@$mSiO_2$ is positive at low pH (pH = 2) and becomes highly negative by increasing the pH to 7 [48]. Therefore, the adsorption capacity of cationic dye MB onto TiON@$mSiO_2$ increased with increasing pH values due to the increase in the electrostatic attraction between the positively charged groups $(=N(CH_3)_2)^+$ of the dyes and the adsorbent surface. No significant change in the surface charge of TiON@$mSiO_2$ was observed with further increase in the solution pH above 7, thus, the adsorption of cationic MB dye did not change significantly at higher pH, this result matched with previous studies [52-55]. Accordingly, by taking in account environmental aspects, a solution pH of 7 was chosen for the further kinetic and isotherm experiments.

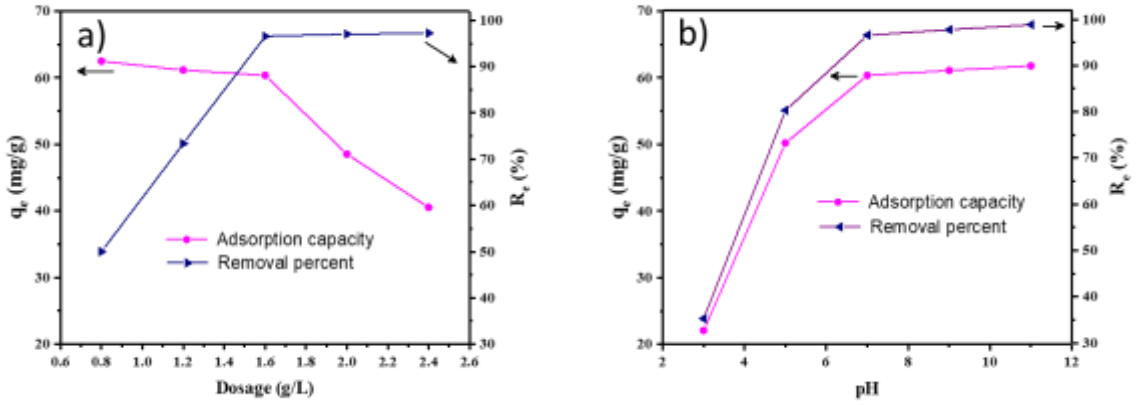

Figure 8: Effect of adsorbent dose at pH 7 (a) and solution pH at dosage of 1.6 g/L (b) on the adsorption capacity (solid circles) and removal (solid triangles) of MB dye onto TiON@$mSiO_2$ sample at room temperature and contact time of 2 h.

3.4. Adsorption isotherms

Four adsorption isotherms of MB dye adsorbed onto the TiON@$mSiO_2$ sample at equilibrium, namely, Langmuir, Freundlich, Dubinin–Radushkevich (D–R) and Tempkin isotherms were used to fit the experimental data by nonlinear regression analysis as shown in Figure 9. The constants and adsorption parameters calculated for four isotherm models according to Eq. (S1-S4, ESI) as well as the determination coefficients (R^2) values of the fitting are listed in

Table 2. The Langmuir model, which assumes that a monolayer adsorption process occurs on the homogeneous surface of an adsorbent without considering the interaction between adsorbate molecules, results in the best fit with a high determination coefficient R^2 of 0.999. On the other hand, the Freundlich model (Figure 9), which assumes a multilayer adsorption process on a heterogeneous surface [34], gives lower R^2 (0.862) value in comparison with that of Langmuir isotherms (

Table 2). In order to determine the type of adsorption process (i.e. chemical or physical process) of MB dye onto TiON@$mSiO_2$, the Dubinin–Radushkevich (D–R) isotherm [56] was also applied. This model is frequently used to distinguish the physical and chemical adsorption of an adsorbate with its mean adsorption free energy, which can be calculated according to Eq. (S4, ESI). Moreover, the maximum adsorbed quantity of MB dye onto TiON@$mSiO_2$ sample can be also determined by using Eq. (S4, ESI). As shown in Figure 9 and

Table 2, the fitting of experimental data using the D-R model resulted in a good determination coefficient R^2 = 0.95 and low value of mean adsorption free energy, E = 0.53 KJ/mol, suggesting a physisorption process. Finally, the Tempkin isotherm is also used to study the adsorbent–adsorbate interactions during the adsorption process. This model assumes a linear decrease in the heat of adsorption for all molecules in the layer with coverage, which is attributed to adsorbate–adsorbent interactions. The adsorption heat $b = -\Delta H$ of the adsorbates (dyes) molecules and Tempkin isotherm equilibrium binding constant K_T (L/mg) corresponding to the maximum binding energy can be calculated from this model according to Eq. (S3, ESI). As shown in Figure 9 and

Table 2, the experimental adsorption data does not fit well with the Tempkin isotherm model and the R^2 = 0.915 is less than those of Langmuir and Dubinin–Radushkevich models. However, the positive value of adsorption heat b calculated from this model indicates that the adsorption process is exothermic [51].

The Langmuir isotherm model best describes the equilibrium adsorption process of MB dye onto TiON@mSiO$_2$ sample by comparing the values of R^2 for four isotherm models (

Table 2). The calculated maximum adsorbed quantity q_{max} of MB is 129 mg/g, which is much higher than that of the other adsorbents (Table 3). Therefore, TiON@mSiO$_2$ can be an effective adsorbent for organic dyes such as MB.

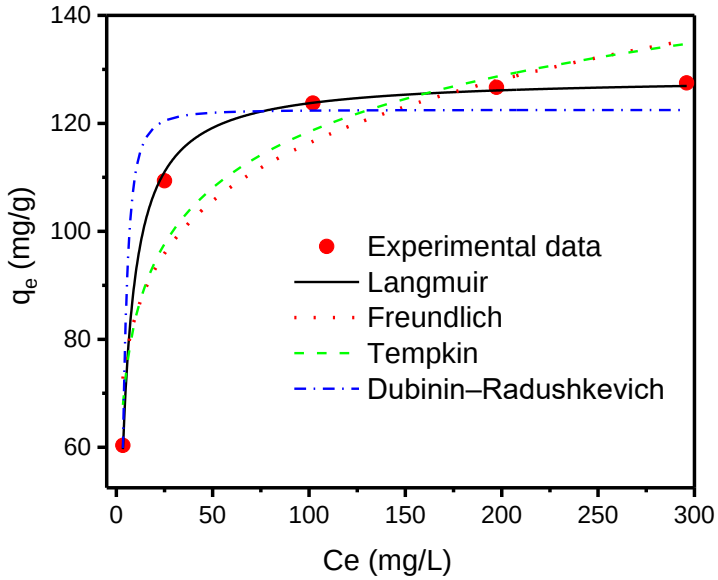

Figure 9: Nonlinear Langmuir, Freundlich, Tempkin and Dubinin–Radushkevich isotherm models for adsorption of MB dye onto TiON@mSiO$_2$ sample (pH = 7, C_i = 100-500 mg/L, Dosage = 1.6 g/L, t = 2 h). The lines represent the nonlinear fitting of the experimental data.

Table 2. The adsorption isotherm parameters for the adsorption of MB dye onto TiON@mSiO$_2$ sample according to nonlinear Langmuir, Freundlich, D-R model, and Temkin models.

Isotherm models	**Parameters**	**Value of parameters**
Langmuir	q_{max} (mg/g)	129
	k_L (L/mg)	0.252
	R^2	0.999
Freundlich	k_F ((mg/g)(L/mg)$^{1/n}$)	61.2
	n	7.2
	R^2	0.862
Temkin	k_T (L/mg)	26.87
	b (kJ/mol)	0.165

	R^2	0.915
D-R	q_m (mg/g)	122
	k_D (mol^2/kJ^2)	1.78×10^{-6}
	E (kJ/mol)	0.53
	R^2	0.95

Table 3. Comparison of adsorption capabilities of TiON@mSiO$_2$ at room temperature with other adsorbents for MB.

Adsorbent	q_{max} **(mg/g)**	**Ref**
MCM-41	74	[26]
TiO_2/MCM-41	54	[26]
Tungstophosphoric acid/TiO_2	50	[26]
Tungstophosphoric acid@TiO_2 /MCM-41	62	[26]
Beta-cyclodextrin silica nano hallow sphere	92	[57]
Fe_3O_4@metal-organic frameworks (MIL-100)	49	[27]
Chitosan and sepiolite clay composite	41	[58]
Reed biochar – hydroxyapatite	21	[59]
SnO_2 quantum dots decorated silica nanoparticles	73	[28]
Co_3O_4/SiO_2 nanocomposite	54	[60]
Polyvinyl alcohol (PVA)	123	[61]
TiON@mSiO$_2$	129	This work

3.5. Thermodynamic studies

In order to study the influence of temperature on the adsorption process of MB dye onto TiON@mSiO$_2$ as well as to determine whether this adsorption process is exothermic or endothermic in nature, thermodynamic studies were performed. The Gibbs free energy (ΔG^0) was calculated according to the eq. S6 (ESI), while, the enthalpy (ΔH^0) and entropy (ΔS^0) were calculated by plotting LnK_d as function of 1/T according to the van't Hoff equation eq. S7 (ESI) [37]. The linear fitting yielded a high regression coefficient (R^2 = 0.995) and the obtained values are listed in Table 4.

As shown in Table 4, the obtained values of Gibbs free energy change ΔG^0 are negative and increase with temperature, which indicates that the adsorption of MB dye molecules onto

TiON@$mSiO_2$ is spontaneous in nature and becomes less favourable with increasing temperature. Moreover, the negative values of enthalpy (ΔH^0) and entropy (ΔS^0) confirm the exothermic nature of this adsorption process as revealed from Tempkin isotherm analysis. This exothermic adsorption process was also observed in the removal of MB by SnO_2 quantum dots decorated silica nanoparticles [28].

Table 4. Thermodynamic parameters calculated for the removal of MB dye by the TiON@$mSiO_2$ (C_0 = 100 mg/L, dosage = 1.6 g/L)

Thermodynamic parameters						
ΔG^0 (kJ mol^{-1}) at different T (K)					ΔS^0 ($Jmol^{-1}$ K^{-1})	ΔH^0 (kJ mol^{-1})
298	308	318	328	338		
-7.1	-6.5	-5.4	-4.4	-3.6	-91	-34

3.6. Adsorption kinetics

The influence of contact time on the adsorption capacity of MB dye onto TiON@$mSiO_2$ at room temperature is displayed in Figure S3. The removal efficiency of MB from the aqueous solution reached 84.9% with corresponding adsorption capacities of 53.05 mg/g in the first 20 min. The adsorption process reached equilibrium with removal efficiency of 96.6% within 120 min. The equilibrium adsorption capacities of MB dye onto TiON@$mSiO_2$ was 60.4 mg/g at a contact time of 120 min.

The adsorption mechanism of MB dye onto TiON@$mSiO_2$ was further analyzed using three different kinetic models, namely, pseudo-first-order, pseudo-second–order, the Elovich model as shown in Figure 10. The kinetic constants calculated for the three kinetic models according to the Eq. S9-S11 (ESI) and the determination coefficient (R^2) values of the fitting are listed in Table 5. As shown in Figure 10 and Table 5, the experimental kinetic data are better fitted with the nonlinear form of pseudo-second-order model (R^2>0.9998) in comparison with those of the pseudo-first-order (R^2>0.9972) and the Elovich kinetic models (R^2>0.9991). Furthermore, the calculated value of adsorption capacity (q_e (cal) = 62 mg/g) at equilibrium according to the pseudo-second-order model was found to be in good agreement with the experimental values (see Figure S3). Accordingly, the adsorption of MB dye onto TiON@$mSiO_2$ can be kinetically

well represented by a pseudo-second-order model in which a molecule of MB dye is adsorbed onto two sites of the TiON@mSiO$_2$ surface, while the concentration of dye is constant [62].

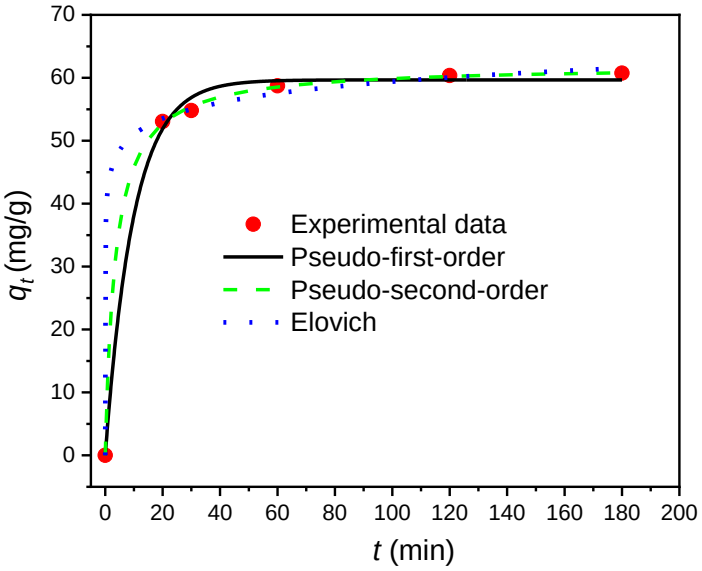

Figure 10: Experimental kinetic data and nonlinear fitted curve with kinetic models of pseudo-first-order (solid line), pseudo-second–order (dashed line), Elovich model (dotted line) for adsorption of MB dye onto TiON@mSiO$_2$ sample at room temperature (pH = 7, C_i = 100 mg/L, Dosage = 1.6 g/L).

Table 5. The adsorption kinetics parameters for the adsorption of MB dye onto TiON@mSiO$_2$ sample with pseudo-first-order, pseudo-second–order, Elovich model and intra-particle diffusion models

Kinetics models	**Parameters**	**Value of parameters**
Pseudo-first-order	q_e (cal) (mg/g)	60
	k_1 (1/min)	0.102
	R^2	0.9972
Pseudo-second-order	q_e (cal) (mg/g)	62
	k_2 (g/(mg.min))	4.6 x 10^{-3}
	R^2	0.9998

Elovich	α (mg/(g.min))	43.4×10^{4}
	β (g/mg)	27.4×10^{-2}
	R^2	0.9991

3.7. FTIR study of methylene blue adsorption

The FTIR spectra of TiON@mSiO$_2$, methylene blue and TiON@mSiO$_2$ after methylene blue adsorption and pure methylene blue are shown in Figure 11. As shown in Figure 11 a, the TiON@mSiO$_2$ sample exhibits similar vibrational band characteristic of mesoporous MCM-41 [63]. The absorption bands at 3450 and 1637 cm^{-1} corresponds to the stretching and bending vibration of O-H group, respectively, which is due to the H_2O molecules on the surface. The peaks at 2978 and 1418 cm^{-1} attributed to the stretching and bending modes of the C–H groups, respectively, which originates from the residual organic precursor used in PECVD process. The absorption bands at 1235 and 1086 cm^{-1} are due to the asymmetric stretching vibrations of the Si–O–Si groups, while, the peaks at 798 and 578 cm^{-1} are attributed to the symmetric stretching modes of Si–O–Si groups. The absorption band at 969 corresponds to the silanol Si-OH group, whereas the peak at 467 cm^{-1} is due to the bending vibration of O–Si–O group. On the other hand, the FTIR spectrum of MB dyes (Figure 11 c) reveals absorption bands corresponding to its main functional groups such as N-H and O-H stretching vibrations at about 3450-3410 cm^{-1}, C=N and C=C stretching vibrations at 1402-1605 cm^{-1}, C-H (methyl) vibration at 1493 cm^{-1}, -CH_3 symmetric deformation at 1350 cm^{-1}, aromatic-nitrogen bond (Ar-N) at 1250 cm^{-1}, C-S vibration at 1142 cm^{-1} and C-H (aromatic) vibration at 896 cm^{-1} [64]. As it can be seen from Figure 11 b, these characteristic bands of MB are observed in the spectrum of TiON@mSiO$_2$ after methylene blue adsorption. Moreover, some absorption peaks TiON@mSiO$_2$ adsorbent such as that corresponding to Si-OH are shifted to lower wavenumber, which suggests the hydrogen bonding between MB and the mesoporous silica. These findings point out that chemical adsorption might be involved in the adsorption process.

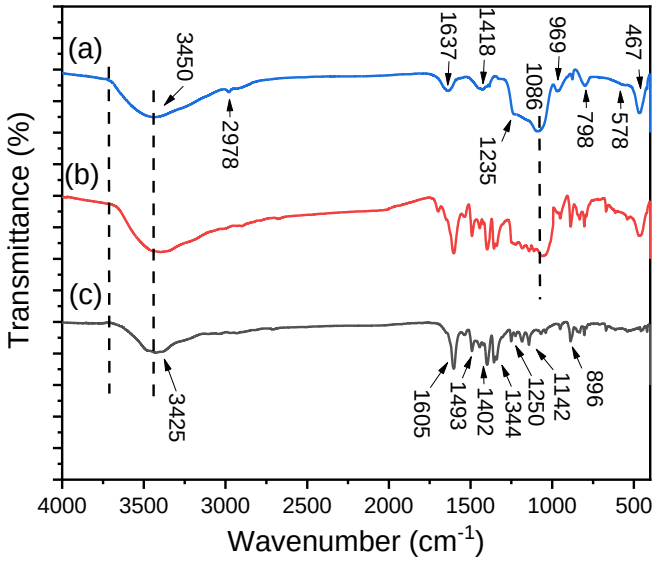

Figure 11: FTIR spectra of (a) TiON@mSiO$_2$, (b) TiON@mSiO$_2$ after methylene blue adsorption and (c) pure methylene blue.

4. Conclusion

In this study, novel TiO$_2$@mSiO$_2$ and TiON@mSiO$_2$ nanocomposites with high surface area were successfully manufactured by PECVD at low temperature (150 °C) and short production time (1 h). The deposition of TiO$_2$ and TiON on the surface of the MCM pores was confirmed by SAXRD, BET and Zeta-potential measurements. The mesoporous structure MCM-41 was retained after the deposition TiO$_2$ and TiON on the surface, but the pore size, pore volume and BET surface area decreased. The grafting of mSiO$_2$ by TiON was tested as an effective adsorbent for methylene blue (MB) dye from aqueous solutions. The adsorption capacity increased with increasing solution pH, and decreased with increasing adsorbent dose. The adsorption equilibrium isotherm is well represented by the Langmuir model and the determined maximum capacity q_{max} (129 mg/g) was much higher than that of the other silica adsorbents reported in previous studies. The negative values of ΔG^0 and ΔH^0 indicate that the adsorption process is exothermic and more energetically favourable. This study shows that the TiON@MCM-41 could be a promising adsorbent for the removal of toxic organic dyes in wastewater.

Acknowledgments

This work was supported by the French Government through a fellowship granted by the French Embassy in Egypt (Institut Français d'Egypte). We would like to kindly thank Maria Unterweger for SAXRD measurements and EPRI-Nanotechnology Center for Zeta potential measurements, TEM measurements and for nitrogen sorption measurements. M. F. Bekheet thanks the Deutscher Akademischer Austauschdienst (DAAD) for the fellowship support at the University of Utah.

Reference

[1] Sandoval A, Hernandez-Ventura C, Klimova TE. Titanate nanotubes for removal of methylene blue dye by combined adsorption and photocatalysis. Fuel. 2017;198:22-30.

[2] Sukriti, Sharma J, Chadha AS, Pruthi V, Anand P, Bhatia J, et al. Sequestration of dyes from artificially prepared textile effluent using RSM-CCD optimized hybrid backbone based adsorbent-kinetic and equilibrium studies. J Environ Manage. 2017;190:176-87.

[3] Aravind P, Selvaraj H, Ferro S, Sundaram M. An integrated (electro- and bio-oxidation) approach for remediation of industrial wastewater containing azo-dyes: Understanding the degradation mechanism and toxicity assessment. J Hazard Mater. 2016;318:203-15.

[4] Long YK, Xiao L, Cao QH. Co-polymerization of catechol and polyethylenimine on magnetic nanoparticles for efficient selective removal of anionic dyes from water. Powder Technol. 2017;310:24-34.

[5] Li D-q, Wang J, Guo Z-g, Li J, Shuai J. Pectin gels cross-linked by Ca2+: An efficient material for methylene blue removal. Journal of Molecular Liquids. 2017;238:36-42.

[6] Anastopoulos I, Hosseini-Bandegharaei A, Fu J, Mitropoulos AC, Kyzas GZ. Use of nanoparticles for dye adsorption. Journal of Dispersion Science and Technology. 2018;39:836-47.

[7] Yusni EM, Tanaka S. Removal behaviour of a thiazine, an azo and a triarylmethane dyes from polluted kaolinitic soil using electrokinetic remediation technology. Electrochim Acta. 2015;181:130-8.

[8] Dang TD, Banerjee AN, Tran QT, Roy S. Fast degradation of dyes in water using manganese-oxide-coated diatomite for environmental remediation. J Phys Chem Solids. 2016;98:50-8.

[9] Samal K, Das C, Mohanty K. Eco-friendly biosurfactant saponin for the solubilization of cationic and anionic dyes in aqueous system. Dyes Pigments. 2017;140:100-8.

[10] Sun Q, Saratale RG, Saratale GD, Kim D-S. Pristine and modified radix Angelicae dahuricae (Baizhi) residue for the adsorption of methylene blue from aqueous solution: A comparative study. Journal of Molecular Liquids. 2018.

[11] Zhang B, Dong ZH, Sun DJ, Wu T, Li YJ. Enhanced adsorption capacity of dyes by surfactant-modified layered double hydroxides from aqueous solution. J Ind Eng Chem. 2017;49:208-18.

[12] El-Sayed M, Nada AA. Polyethylenimine −functionalized amorphous carbon fabricated from oil palm leaves as a novel adsorbent for Cr(VI) and Pb(II) from aqueous solution. Journal of Water Process Engineering. 2017;16:296-308.

[13] El-Maghrabi HH, Abdelmaged SM, Nada AA, Zahran F, El-Wahab SA, Yahea D, et al. Magnetic graphene based nanocomposite for uranium scavenging. J Hazard Mater. 2017;322:370-9.

[14] Bensalah H, Bekheet MF, Younssi SA, Ouammou M, Gurlo A. Removal of cationic and anionic textile dyes with Moroccan natural phosphate. J Environ Chem Eng. 2017;5:2189-99.

[15] Huang WY, Zhang YM, Li D. Adsorptive removal of phosphate from water using mesoporous materials: A review. J Environ Manage. 2017;193:470-82.

[16] Cui HZ, Li YL, Liu S, Zhang JF, Zhou Q, Zhong R, et al. Novel Pb(II) ion-imprinted materials based on bis-pyrazolyl functionalized mesoporous silica for the selective removal of Pb(II) in water samples. Micropor Mesopor Mat. 2017;241:165-77.

[17] Fellenz N, Perez-Alonso FJ, Martin PP, Garcia-Fierro JL, Bengoa JF, Marchetti SG, et al. Chromium (VI) removal from water by means of adsorption-reduction at the surface of amino-functionalized MCM-41 sorbents. Micropor Mesopor Mat. 2017;239:138-46.

[18] Abdel Salam MS, Betiha MA, Shaban SA, Elsabagh AM, Abd El-Aal RM, El kady FY. Synthesis and characterization of MCM-41-supported nano zirconia catalysts. Egyptian Journal of Petroleum.24:49-57.

[19] Karakhanov EA, Glotov AP, Nikiforova AG, Vutolkina AV, Ivanov AO, Kardashev SV, et al. Catalytic cracking additives based on mesoporous MCM-41 for sulfur removal. Fuel Process Technol. 2016;153:50-7.

[20] Zhao HR, Zhang T, Dai JX, Jiang K, Fei T. Preparation of hydrophilic organic groups modified mesoporous silica materials and their humidity sensitive properties. Sensor Actuat B-Chem. 2017;240:681-8.

[21] Guan Y, Wang SM, Wang X, Sun C, Huang Y, Liu C, et al. In situ self -assembled synthesis of Ag-AgBr/Al-MCM-41 with excellent activities of adsorption-photocatalysis. Appl Catal B-Environ. 2017;209:329-38.

[22] Zarrabi M, Entezari MH, Goharshadi EK. Photocatalytic oxidative desulfurization of dibenzothiophene by C/TiO2@MCM-41 nanoparticles under visible light and mild conditions. Rsc Adv. 2015;5:34652-62.

[23] Guo YG, Liu DF, Zhao Y, Gong B, Guo YJ, Huang WL. Synthesis of chitosan-functionalized MCM-41-A and its performance in Pb(II) removal from synthetic water. J Taiwan Inst Chem E. 2017;71:537-45.

[24] Fan JW, Wang XM, Teng W, Yang JP, Ran XQ, Gou X, et al. Phenyl-functionalized mesoporous silica materials for the rapid and efficient removal of phthalate esters. J Colloid Interf Sci. 2017;487:354-9.

[25] Melendez-Ortiz HI, Perera-Mercado Y, Mercado-Silva JA, Olivares-Maldonado Y, Castruita G, Garcia-Cerda LA. Functionalization with amine-containing organosilane of mesoporous silica MCM-41 and MCM-48 obtained at room temperature. Ceram Int. 2014;40:9701-7.

[26] Zanjanchi MA, Golmojdeh H, Arvand M. Enhanced adsorptive and photocatalytic achievements in removal of methylene blue by incorporating tungstophosphoric acid-TiO2 into MCM-41. J Hazard Mater. 2009;169:233-9.

[27] Shao YM, Zhou LC, Bao C, Ma JJ, Liu MZ, Wang F. Magnetic responsive metal-organic frameworks nanosphere with core-shell structure for highly efficient removal of methylene blue. Chem Eng J. 2016;283:1127-36.

[28] Dutta D, Thakur D, Bahadur D. SnO2 quantum dots decorated silica nanoparticles for fast removal of cationic dye (methylene blue) from wastewater. Chem Eng J. 2015;281:482-90.

[29] An YL, Song WL, Wei P, Fan MQ, Chen HC, Ju QJ, et al. Polyaniline-wrapping hollow sulfur with MCM-41 template and improved capacity and cycling performance of lithium sulfur batteries. Renew Energ. 2016;99:289-94.

[30] Wang SH, Wang KH, Jehng J, Liu LC. Preparation of TiO2/MCM-41 by plasma enhanced chemical vapor deposition method and its photocatalytic activity. Front Env Sci Eng. 2012;6:304-12.

[31] Singh UG, Williams RT, Hallam KR, Allen GC. Synthesis and characterisation of titanium and titanium nitride-functionalised MCM 41 materials. Solid State Sci. 2005;7:1104-12.

[32] Grun M, Unger KK, Matsumoto A, Tsutsumi K. Novel pathways for the preparation of mesoporous MCM-41 materials: control of porosity and morphology. Micropor Mesopor Mat. 1999;27:207-16.

[33] Langmuir I. The Constitution And Fundamental Properties Of Solids And Liquids. Part I. Solids. Journal of the American Chemical Society. 1916;38:2221-95.

[34] Freundlich HMF. Uber die adsorption in losungen. Z Phys Chem. 1906;57:385-470.

[35] Tempkin MI, Pyzhev V. Kinetics of ammonia synthesis on promoted iron catalyst. Acta Phys Chim USSR,. 1940;12:327-56.

[36] Redlich O, Peterson DL. A Useful Adsorption Isotherm. J Phys Chem-Us. 1959;63:1024-.

[37] Tran HN, You SJ, Hosseini-Bandegharaei A, Chao HP. Mistakes and inconsistencies regarding adsorption of contaminants from aqueous solutions: A critical review. Water Res. 2017;120:88-116.

[38] Lagergren S. About the theory of so-called adsorption of soluble substances. K Sven Vetensk Handl 24:1-39.

[39] Blanchard G, Maunaye M, Martin G. Removal of Heavy-Metals from Waters by Means of Natural Zeolites. Water Res. 1984;18:1501-7.

[40] Roginsky S, Zeldovich YB. The catalytic oxidation of carbon monoxide on manganese dioxide. Acta Phys Chem USSR. 1934;1:554.

[41] Kresge CT, Leonowicz ME, Roth WJ, Vartuli JC, Beck JS. Ordered Mesoporous Molecular-Sieves Synthesized by a Liquid-Crystal Template Mechanism. Nature. 1992;359:710-2.

[42] Sing KSW, Everett DH, Haul RAW, Moscou L, Pierotti RA, Rouquerol J, et al. Reporting Physisorption Data for Gas Solid Systems with Special Reference to the Determination of Surface-Area and Porosity (Recommendations 1984). Pure Appl Chem. 1985;57:603-19.

[43] Thommes M. Physical Adsorption Characterization of Nanoporous Materials. Chem-Ing-Tech. 2010;82:1059-73.

[44] Sanjines R, Tang H, Berger H, Gozzo F, Margaritondo G, Levy F. Electronic-Structure of Anatase Tio2 Oxide. J Appl Phys. 1994;75:2945-51.

[45] Youssef L, Leoga AJK, Roualdes S, Bassil J, Zakhour M, Rouessac V, et al. Optimization of N-doped TiO2 multifunctional thin layers by low frequency PECVD process. Journal of the European Ceramic Society. 2017;37:5289-303.

[46] Huang L, Xiao H, Ni Y. Cationic MCM-41: synthesis, characterization and sorption behavior towards aromatic compounds. Colloid Surface A. 2004;247:129-36.

[47] Tanaka KI, Ozaki A. Acid-Base Properties and Catalytic Activity of Solid Surfaces. J Catal. 1967;8:1-&.

[48] Miyauchi M, Ikezawa A, Tobimatsu H, Irie H, Hashimoto K. Zeta potential and photocatalytic activity of nitrogen doped TiO2 thin films. Phys Chem Chem Phys. 2004;6:865-70.

[49] Mohammed RR, Ketabchi MR, McKay G. Combined magnetic field and adsorption process for treatment of biologically treated palm oil mill effluent (POME). Chem Eng J. 2014;243:31-42.

[50] Wang JS, Peng RT, Yang JH, Liu YC, Hu XJ. Preparation of ethylenediamine-modified magnetic chitosan complex for adsorption of uranyl ions. Carbohyd Polym. 2011;84:1169-75.

[51] Du QJ, Sun JK, Li YH, Yang XX, Wang XH, Wang ZH, et al. Highly enhanced adsorption of congo red onto graphene oxide/chitosan fibers by wet-chemical etching off silica nanoparticles. Chem Eng J. 2014;245:99-106.

[52] Heidarinejad Z, Rahmanian O, Fazlzadeh M, Heidari M. Enhancement of methylene blue adsorption onto activated carbon prepared from Date Press Cake by low frequency ultrasound. Journal of Molecular Liquids. 2018.

[53] Guesmi Y, Agougui H, Lafi R, Jabli M, Hafiane A. Synthesis of hydroxyapatite-sodium alginate via a co-precipitation technique for efficient adsorption of Methylene Blue dye. Journal of Molecular Liquids. 2018;249:912-20.

[54] Ezzeddine Z, Batonneau-Gener I, Pouilloux Y, Hamad H. Removal of methylene blue by mesoporous CMK-3: Kinetics, isotherms and thermodynamics. Journal of Molecular Liquids. 2016;223:763-70.

[55] Siddiqui SI, Rathi G, Chaudhry SA. Acid washed black cumin seed powder preparation for adsorption of methylene blue dye from aqueous solution: Thermodynamic, kinetic and isotherm studies. Journal of Molecular Liquids. 2018;264:275-84.

[56] Calagui MJC, Senoro DB, Kan CC, Salvacion JWL, Futalan CM, Wan MW. Adsorption of indium(III) ions from aqueous solution using chitosan-coated bentonite beads. J Hazard Mater. 2014;277:120-6.

[57] Ebadi A, Rafati AA. Preparation of silica mesoporous nanoparticles functionalized with beta-cyclodextrin and its application for methylene blue removal. Journal of Molecular Liquids. 2015;209:239-45.

[58] Marrakchi F, Khanday WA, Asif M, Hameed BH. Cross-linked chitosan/sepiolite composite for the adsorption of methylene blue and reactive orange 16. Int J Biol Macromol. 2016;93:1231-9.

[59] Li Y, Zhang Y, Wang G, Li S, Han R, Wei W. Reed biochar supported hydroxyapatite nanocomposite: Characterization and reactivity for methylene blue removal from aqueous media. Journal of Molecular Liquids. 2018.

[60] Abdel Ghafar HH, Ali GA, Fouad OA, Makhlouf SA. Enhancement of adsorption efficiency of methylene blue on Co3O4/SiO2 nanocomposite. Desalination and Water Treatment. 2015;53:2980-9.

[61] Agarwal S, Sadegh H, Monajjemi M, Hamdy AS, Ali GA, Memar AO, et al. Efficient removal of toxic bromothymol blue and methylene blue from wastewater by polyvinyl alcohol. Journal of Molecular Liquids. 2016;218:191-7.

[62] Ho YS, McKay G. Pseudo-second order model for sorption processes. Process Biochem. 1999;34:451-65.

[63] Shankar H, Rajasudha G, Karthikeyan A, Narayanan V, Stephen A. Synthesis, characterization and photocatalytic activity of nanotitania loaded W-MCM-41. Nanotechnology. 2008;19.

[64] Yao H, Li N, Xu S, Xu JZ, Zhu JJ, Chen HY. Electrochemical study of a new methylene blue/silicon oxide nanocomposition mediator and its application for stable biosensor of hydrogen peroxide. Biosens Bioelectron. 2005;21:372-7.